# Supplementary Information

# Structure and reactivity of a mononuclear non-haem iron(III)–peroxo complex

Jaeheung Cho[1], Sujin Jeon[1], Samuel A. Wilson[2], Lei V. Liu[2], Eun A Kang[1], Joseph J. Braymer[3], Mi Hee Lim[3], Britt Hedman[4], Keith O. Hodgson[2,4], Joan Selverstone Valentine[1,5]*, Edward I. Solomon[2,4]* & Wonwoo Nam[1]*

[1]Department of Bioinspired Science, Department of Chemistry and Nano Science, Center for Biomimetic Systems, Ewha Womans University, Seoul 120-750, Korea

[2]Department of Chemistry, Stanford University, Stanford, CA 94305, USA

[3]Department of Chemistry, University of Michigan, Ann Arbor, MI 48109-2216, USA

[4]Stanford Synchrotron Radiation Lightsource, SLAC National Accelerator Laboratory, Stanford University, Menlo Park, CA 94025-7015, USA

[5]Department of Chemistry and Biochemistry, UCLA, Los Angeles, CA 90095-1569, USA

*Corresponding authors: jsv@chem.ucla.edu, edward.solomon@stanford.edu, wwnam@ewha.ac.kr

## Table of Contents

**Experimental Section (Supplementary):**

**Materials and Instrumentation.** All chemicals obtained from Aldrich Chemical Co. were the best available purity and used without further purification unless otherwise indicated. Solvents were dried according to published procedures and distilled under Ar prior to use (*S1*). $H_2{}^{18}O_2$ (90% $^{18}O$-enriched, 2% $H_2{}^{18}O_2$ in water) and $^{18}O_2$ (60% $^{18}O$-enriched) were purchased from ICON Services Inc. (Summit, NJ, USA). [Fe(II)(TMC)$(CF_3SO_3)_2$], $[Fe(III)(TMC)(OO)]^+$ (**1**), and $[Fe(IV)(TMC)(O)(CH_3CN)]^{2+}$ (**3**) were prepared according to the literature methods (*S2, S3*). $[Fe(III)(TMC)(^{18}O^{18}O)]^+$ was prepared by adding 5 equiv $H_2{}^{18}O_2$ (8 μL, 90% $^{18}O$-enriched, 2% $H_2{}^{18}O_2$ in water) to a solution containing $[Fe(II)(TMC)]^{2+}$ (1 mM) and 2 equiv triethylamine (TEA) in $CF_3CH_2OH$ (2 mL) at –40 $^oC$.

UV-vis spectra were recorded on a Hewlett Packard 8453 diode array spectrophotometer equipped with a UNISOKU Scientific Instruments for low-temperature experiments or with a circulating water bath. Fast reactions were monitored using a Hi-Tech Scientific SF-61 DX2 cryogenic stopped-flow spectrometer equipped with a Xe arc lamp and a KinetaScan diode array rapid scanning unit. Electrospray ionization mass spectra (ESI MS) were collected on a Thermo Finnigan (San Jose, CA, USA) LCQ$^{TM}$ Advantage MAX quadrupole ion trap instrument, by infusing samples directly into the source using a manual method. The spray voltage was set at 4.2 kV and the capillary temperature at 80 °C. Product analysis was performed with an Agilent Technologies 6890N gas chromatograph (GC) and Thermo Finnigan (Austin, Texas, USA) FOCUS DSQ (dual stage quadrupole) mass spectrometer interfaced with Finnigan FOCUS gas chromatograph (GC-MS). EPR spectra were taken at 10 K using a X-band Bruker EMX-plus spectrometer

equipped with a dual mode cavity (ER 4116DM). Low temperature was achieved and controlled with an Oxford Instruments ESR900 liquid He quartz cryostat with an Oxford Instruments ITC503 temperature and gas flow controller. Crystallographic analysis was conducted with a Bruker SMART APEX CCD equipped with a Mo X-ray tube at the Crystallographic Laboratory of Ewha Womans University.

**Generation and Characterization of [Fe(III)(TMC)(OOH)]$^{2+}$ (2)**. Treatment of [Fe(III)(TMC)(OO)]$^{+}$ (**1**) (1 mM) with 3 equiv $HClO_4$ in acetone/$CF_3CH_2OH$ (3:1) or acetone (2 mL) at –40 $^{o}$C afforded the formation of a violet solution. Titration experiments showed that 3 equiv $HClO_4$ are required for the full formation of **2**. Spectroscopic data, including UV-vis, EPR, and resonance Raman, are reported in Fig. 3 and Supplementary Figs. S9 and S11. Isotopically labeled **2**, [Fe(III)(TMC)($^{18}O^{18}OH$)]$^{2+}$, was prepared by adding 3 equiv $HClO_4$ to a solution containing [Fe(III)(TMC)($^{18}O^{18}O$)]$^{+}$ (1 mM) in acetone/$CF_3CH_2OH$ (3:1) (2 mL) at –40 $^{o}$C.

**X-ray Crystallography.** Crystals suitable for X-ray analysis were successfully grown by storing a solution of **1** with excess $NaClO_4$ in $CH_3OH$/diethyl ether (1:1) at –40 ºC, and the yield of crystals was ~80%. A single crystal of [Fe(TMC)(OO)]($ClO_4$) (**1**-($ClO_4$)) was picked from solutions by a nylon loop (Hampton Research Co.) on a hand made cooper plate mounted inside a liquid $N_2$ Dewar vessel at *ca*. –40 ºC and mounted on a goniometer head in a $N_2$ cryostream. Data collections were carried out on a Bruker SMART AXS diffractometer equipped with a monochromator in the Mo Kα (λ = 0.71073 Å) incident beam. The CCD data were integrated and scaled using the Bruker-SAINT software package, and the structure was solved and refined using SHEXTL V 6.12 (*S4*). Hydrogen atoms were located in the calculated positions. Crystal data for **1**-($ClO_4$): $C_{14}H_{32}ClFeN_4O_6$, *Monoclinic*,

*P2(1)*, Z = 2, $a$ = 8.2773(14), $b$ = 14.502(3), $c$ = 8.7454(15) Å, $\beta$ = 110.833(9), $V$ = 981.2(3) Å$^3$, $\mu$ = 0.942 mm$^{-1}$, $d_{calc}$ = 1.502 g/cm$^3$, $R_1$ = 0.0597, $wR_2$ = 0.1541 for 3708 unique reflections, 239 variables. The crystallographic data for **1**-($ClO_4$) are listed in Supplementary Table 1, and Supplementary Table 2 lists the selected bond distances and angles. CCDC-804038 for **1**-($ClO_4$) contains the supplementary crystallographic data for this paper. These data can be obtained free of charge via www.ccdc.cam.ac.uk/data_request/cif (or from the Cambridge Crystallographic Data Centre, 12, Union Road, Cambridge CB2 1EZ, UK; fax: (+44) 1223-336-033; or deposit@ccdc.cam.ac.uk).

**X-ray Absorption Spectroscopy (XAS).** X-ray absorption spectra were recorded at the Stanford Synchrotron Radiation Lightsource (SSRL) on beam line 9-3 (*S5*) over an energy range of 6785 to 8129 eV ($k$ = 16 Å$^{-1}$), under ring conditions of 3.0 GeV, and 300 mA. At 300 mA ring current, substantial photo reduction was observed and thus the beam was detuned 50% at 8129 eV and hutch slits were reduced to 2 x 1 mm size for a total of 6 spots (1 scan/spot) per each 2 x 10 mm cell. For each data set, a minimum of 6 scans were collected (typically 10 – 15 scans), across multiple cells. During collection, data were continuously monitored in order to insure sample homogeneity across the multiple spots and cells. Complete data sets were collected on **1**, **2**, and **3** in acetone, acetone/$CF_3CH_2OH$, and acetonitrile (**1** and **2** only). Data on [Fe(IV)(TMC)(O)($CH_3CN$)]$^{2+}$ prepared via oxo-transfer had been collected previously.

Fluorescence data were collected using a solid-state 100-element Ge detector (*S6*) with 3μM Mn filter and Soller slits aligned at 90º, with sample orientated at 45º to incident beam and the first inflection point of the Fe foil set to 7111.2 eV as an internal calibration

(*S7*). Sample temperature was maintained at 10 K using an Oxford Instruments CF1208 continuous-flow liquid helium cryostat.

Reduction and normalization of the data were performed according to established methods (*S8*-*S10*) using the program PySpline (*S11*) for background subtraction and spline fitting. In order to compare multiple data sets, each set was truncated to $k = 9.5$ Å$^{-1}$ for pre-edge and edge analysis. The pre-edge data ($k = 9.5$ Å$^{-1}$) were normalized using a third-order post-edge polynomial background and a two-segment spline. The full ($k = 16$ Å$^{-1}$) EXAFS data were fit using a second-order post-edge polynomial and 4-segment spline for comparison to one another, and then were then truncated based on the useable portion and re-splined for use in the final fit.

Using the fitting program EDG_FIT (*S12*), the Fe K pre-edge features were successfully modeled using a pseudo-Voigt lineshape in a 50:50 ratio of Lorentzian:Gaussian functions. The energy position, full width at half-maximum (FWHM), and peak intensity were all allowed to vary throughout the fitting process. A function modeling the background was empirically chosen to give the best fit. For a fit to be acceptable, it had to reasonably match both the pre-edge data as well as that of the second derivative. In all cases, three acceptable fits with different FWHM (± 0.5 fixed from float) backgrounds were acquired over the energy ranges of 7108-7117, 7108-7118, and 7108-7119 eV resulting in a total of nine pre-edge fits per data set, which were averaged to get mean values. Standard deviations for the peak energies and intensities were used to quantify the error.

EXAFS signals were calculated using FEFF (version 7.0) from the X-ray crystal structure of **1** and DFT optimized structures for **2** and **3**. The models were fit using OPT as

part of the program suite EXAFSPAK (*S13*). During the fitting, the bond lengths (R) and bond variance ($\sigma^2$) were allowed to float. The shift in threshold energy ($k$ = 0, $E_0$) was also varied but constrained as a common variable ($\Delta E_0$) for all fit paths for a given data set. The amplitude reduction factors ($S_0^2$) were fixed to a value of 1.0 and coordination numbers (N) were varied systematically to accomplish the best fit to the data based on the model. The best overall fit was evaluated based on comparison of the normalized error (F) for each proposed fit and by inspection of the fit to the EXAFS data, Fourier transform, individual EXAFS wave components, and comparative Fe K pre-edge intensities. Based on EXAFS studies of known complexes, the uncertainties in final distances are within 0.02 Å.

**Resonance Raman Spectroscopy.** Resonance Raman (rR) spectra were obtained using a triple monochromator (Spex 1877 CP) with 1200, 1800, and 2400 grooves/mm holographic spectrograph gratings and an Andor iDus DU420A BR-DD CCD detector cooled to −80 °C. Excitation was provided by Kr (Coherent I90C-K) ion, Ar (Innova Sabre 25/7) ion, and Ti-Sapphire (Coherent 890) lasers with incident power in the 60-300 mW range using an ~135° backscattering configuration. Samples were prepared in $d_6$-acetone with 5 mM Fe concentration in NMR tubes cooled to 77 K in a liquid nitrogen finger dewar (Wilmad).

**Density Functional Theory (DFT).** Spin-unrestricted DFT calculations were performed with the Gaussian 09 package (*S14*). The full TMC ligand was used for all models. The experimentally defined S = 5/2 spin states were evaluated for both the $[Fe(III)(TMC)(OO)]^+$ and $[Fe(III)(TMC)(OOH)]^{2+}$ species. The crystal structure of the $[Fe(III)(TMC)(OO)]^+$ was used as the starting point for both geometry optimizations. Acetone and acetonitrile were each considered as a possible sixth axial ligand for the five-

coordinated $[Fe(III)(TMC)(OOH)]^{2+}$ species, with the TMC methyl groups both *syn* and *anti* to the $OOH^-$ group. For acetone, an initial Fe-$O_{acetone}$ bond length 2.3 Å was specified, while an initial Fe-$N_{acetonitrile}$ bond length of 2.2 Å was used for acetonitrile. Geometry optimization were performed using the hybrid density functional B3LYP with the 6-311G* basis set for Fe and the 6-311G basis set for all other atoms. Frequency calculations were done at the same level of theory to ensure true local minima with no negative eigenvalues. Single point calculations were done at B3LYP/6-311+G** level of theory. Solvation effects were accounted for using a polarized continuum model (PCM) with acetone as the solvent. It was found that acetone does not bind to the Fe for either the *syn* or *anti* configurations of the TMC methyl groups with respect to the $OOH^-$ group. Acetonitrile does bind to the Fe when the methyl groups are in the *anti* configuration but not the *syn* configuration. The same level of theory stated above was used to evaluate the nucleophilic reactivities of the $[Fe(III)(TMC)(OO)]^+$ and $[Fe(III)(TMC)(OOH)]^{2+}$ species with 2-phenylpropionaldehyde (2-PPA).

**Reactivity Studies of 1, 2, and 3.** All reactions were run in a 1-cm UV cuvette by monitoring UV-vis spectral changes of reaction solutions. Rate constants were determined by fitting the changes in absorbance at 782 nm for **1**, 526 nm for **2**, and 823 nm for **3**. Reactions were run at least in triplicate, and these data reported represent the average of these reactions. Complex **2** was prepared by reacting **1** with 3 equiv $HClO_4$ at –40 ºC and used directly in reactivity studies, such as the oxidation of xanthene, 9,10-dihydroanthracene (DHA), 2-phenylpropionaldehyde (2-PPA), and *para*-substituted benzaldehydes, *para*-Y-Ph-CHO (Y = OMe, Me, H, Cl) under stoichiometric conditions in acetone/$CF_3CH_2OH$ (3:1) or acetone at the given temperatures. For the stopped-flow

experiments, the intermediate **2** was generated by rapidly mixing a solution of **1** and 3 equiv $HClO_4$ in acetone/$CF_3CH_2OH$ (3:1) in the initial push of a double-mixing experiment at −40 or −80 ºC. Then, a solution containing substrates was introduced by a second push to initiate the reaction (final mixing concentration of 1 mM for **2**) at the same low temperature. All reaction traces were collected at 526 or 805 nm, using a 1-cm optical path length at given temperature. The raw kinetic data were treated with KinetAsyst 3 (Hi-Tech Scientific) and Specfit/32 Global Analysis System software from Spectrum Software Associates. In order to understand proton effect for the conversion of **2** to **3**, the intermediate **2** (1 mM) was prepared by reacting **1** with 3, 30 and 100 equiv $HClO_4$ in $CH_3CN$ at −40 ºC. The proton effect was investigated using a similar method in acetone/$CF_3CH_2OH$ (3:1), acetone, or $CF_3CH_2OH$ at −20 ºC as well. After the completion of reactions, pseudo-first-order fitting of the kinetic data allows us to determine $k_{obs}$ values (see Supplementary Table 6). For the conversion reactions of **2** to **3** in the presence and absence of substrates, such as ethylbenzene, cyclohexene, 1,4-cyclohexadiene, thioanisole, the intermediate **2** was prepared by reacting **1** (2 mM) and 3 equiv $HClO_4$. Taking cyclohexene as a representative example, reactions for the conversion of **2** to **3** were performed in the presence and absence of 50 equiv cyclohexene in acetone/$CF_3CH_2OH$ (3:1) at −20 ºC or in $CH_3CN$ at −40 ºC. Conversion yields were determined by the comparison of absorbance at 823 nm.

For product analysis, the purity of substrates was checked with GC and GC-MS prior to use. Products were analyzed by injecting the reaction mixture directly into GC and GC-MS. Products were identified by comparing with authentic samples, and product yields were determined by comparison against standard curves prepared with authentic samples

and using decane as an internal standard.

**Results and Discussion (Supplementary):**

**Resonance Raman Results and Analysis for 1.** The intermediate **1** was characterized with resonance Raman (rR) spectroscopy (Supplementary Fig. 3). The rR spectrum of the $^{16}$O-labeled **1** in $d_6$-acetone, obtained by 778-nm excitation at 77 K, shows two peaks that exhibit isotope shifts upon $^{18}$O-substitution (Supplementary Fig. 3). The peak at 487 cm$^{-1}$ shifts to 468 cm$^{-1}$ with a $^{16,18}\Delta$ value of 19 cm$^{-1}$ ($^{16,18}\Delta$ (calcd) = 21 cm$^{-1}$) and is assigned as the Fe−O stretch. The other isotopically sensitive peak is at 825 cm$^{-1}$. In the $^{18}$O-spectrum of **1**, there is a doublet of peaks at 785 and 774 cm$^{-1}$ arising from a Fermi resonance with an intensity-weighted average peak position at 781 cm$^{-1}$. Thus, the $^{16,18}\Delta$ value is 44 cm$^{-1}$ ($^{16,18}\Delta$ (calcd) = 47 cm$^{-1}$) and has been assigned as the O−O stretch. These values are comparable to the Fe−O and O−O stretches in other spectroscopically characterized high-spin side-on Fe(III)-peroxo complexes with heme and nonheme ligands (*S15, S16*). Finally, there is a good correlation between the O-O stretching frequency and the observed O-O bond length in **1** (Supplementary Fig. 4) (*S17*).

**EXAFS Results and Analysis for 1, 2, and 3.** Final EXAFS fits for **1**, **2**, and **3** in acetone, acetone/$CF_3CH_2OH$, and acetonitrile respectively, are given in Supplementary Table 4 and are shown in Supplementary Fig. 22. Although collected to $k$ = 16 Å$^{-1}$, the data were truncated to $k$ = 14 Å$^{-1}$ for the final fit based on quality. **1**, **2**, and **3** were each fit using the same set of EXAFS paths for first, second, and outer shell atoms, based on TMC ligation. The EXAFS data exhibit distinctly different spectra along the reaction coordinate of **1**, to **2**, to **3** as is observed by the shift and change in beat pattern. These changes are

mapped onto the FT which shows a distinct shift to shorter distances (R+Δ) of the main feature in going from 6-coordinate high-spin peroxo, to 5-coordinate high-spin hydroperoxo, to 6-coordinate low-spin Fe(IV)=O.

$[Fe(III)(TMC)(OO)]^+$ (**1**) was best fit (Supplementary Table 4, **1**) using a 2:4 split first shell with two oxygen atoms at a distance of 1.92 Å which is in agreement with the crystallographic data (Fig. 1, Supplementary Table 2). Final fits for **1** were also tested with varied coordination environments including 1:5 and 1:4, but in both cases 2:4 was preferred based on visual fit and lowest error. The second and outer shells were fit with a total of 14 carbon atoms broken into two groups of 8:6 representative of the 10-member cyclam ring and the 4 methyl groups. Due to the rigid ring structure a multiple scattering (MS) path with a coordination number (CN) of 24 was also appropriate. However, due to the large number of carbon atoms at multiple distances from the Fe, the MS path is under fit as a result of its compensation for several different contributions around ~3.3 Å, thus exhibiting a low bond variance of 219.

The final EXAFS fit for $[Fe(III)(TMC)(OOH)]^+$ (**2**) (Supplementary Table 4, **2**) exhibits a distinct change in the coordination environment from a 2:4 first shell in **1** to a 1:4 shell in **2**. The first shell exhibits contracted Fe-ligand distances with a short Fe-O path at 1.85 Å and the remaining Fe-N paths at 2.16 Å consistent with the loss of an Fe-O bond upon going from **1** to **2**. The second and outer shells are fit in an analogous fashion to those of **1** with 14 single scattering (SS) paths divided into two shells representative of the TMC ring and the 4 methyl groups. Bond variances of these shells, as well as the MS contribution are also comparable to those of **1**, defining **2** as a 5-coordinate high-spin ferric-hydroperoxo species.

The complete fit to the EXAFS data for the decay product $[Fe(IV)(TMC)(O)]^{2+}$ (**3**) in acetone (Supplementary Table 4, **3**) shows a coordination environment typical for other low-spin nonheme Fe(IV)=O compounds (*S18-S20*) with a contracted 1:5 split first shell, a short Fe=O bond at 1.67 Å, and the remaining Fe-N ligation at 2.08 Å. The outer shells also exhibit a slight contraction consistent with the higher oxidation state of the iron, and shorter first shell bond lengths at 2.96 Å (8 Fe-C SS), 3.28 Å (24 TMC MS), and 3.36 Å (6 Fe-C SS). The outer shell also shows an increase in the degree of bond variance for all paths, likely a result of increased disorder in the constrained TMC ring upon oxidation to Fe(IV) and contraction of the first shell.

**Conversion of 2 to 3.** EXAFS data were collected on the decay product of **2**, prepared in three different solvents (e.g., acetone, acetone/$CF_3CH_2OH$, and acetonitrile) (Supplementary Fig. 23). Under all three reaction conditions, the EXAFS data for **3** exhibit a contracted first shell with shorter Fe-N TMC bond lengths at 2.08 Å, the formation of a short bond at ~1.67 Å (Supplementary Table 7), and the addition of a sixth ligand, likely from solvent, at least in acetonitrile. The first shell bond lengths are consistent with those of other nonheme Fe(IV)=O compounds (*S20*), specifically $[Fe(IV)(TMC)(O)(CH_3CN)]^{2+}$ and closely related species (*S3, S19*). These data also exhibit an intense Fe K pre-edge of 37.2 units (Fig. 2, Supplementary Table 5) which is comparable to the pre-edge of other $[Fe(IV)(TMC)(O)]^{2+}$ models (*S19*, *S20*) and results from a short Fe–O bond which increases 4p mixing into the 3d manifold. Taken together, these XAS data clearly identify **3** as a low-spin $[Fe(IV)(TMC)(O)]^{2+}$ complex.

**EXAFS Results and Analysis: Solvent Effects on $[Fe(IV)(TMC)(O)]^{2+}$ (3).** Final EXAFS fits for $[Fe(IV)(TMC)(O)]^{2+}$, **3**, in acetone vs. acetonitrile are shown in

Supplementary Fig. 23 and given in Supplementary Table 7, Fit **3A**, **3B/C** along with that of $[Fe(IV)(TMC)(O)(CH_3CN)]^{2+}$ for comparison (Supplementary Table 8, Fit **OT** (OT = Oxo-Transfer)). The EXAFS data and corresponding FT for all three species are very similar except for an increase in outer shell intensity for **3** in acetonitrile, and $[Fe(IV)(TMC)(O)(CH_3CN)]^{2+}$ prepared by the direct oxidation of $[Fe(II)(TMC)]^{2+}$ by single oxygen atom donors, such as iodosylbenzene (PhIO) and peracids (*S3*).

Due to the data quality of **3** in acetonitrile, EXAFS data were truncated to k = 12 $Å^{-1}$ and re-splined with a 3 segment spline. Fit **3A**, Supplementary Table 7 is a reproduction of Fit **3**, Supplementary Table 4 for **3** in acetone, but with the shortened k-range. Bond lengths for all paths remain unchanged (within EXAFS error ± 0.02 Å), with only slight changes in bond variance. Direct comparison of **3** in acetone vs. acetonitrile shows an increase in outer shell intensity between the two (Supplementary Table 8). When the EXAFS data of **3** in acetonitrile are fit using 24 MS contributions from TMC (Fit **3**B, Supplementary Table 7), the results give bond variance values that are artificially low as a result of some unaccounted contribution. As an alternative, fit **3C** was generated using only two intense forward focused MS paths from an axially bound acetonitrile and yet had similar values for bond variance. Thus, in the case of **3** in acetonitrile, the EXAFS data show that acetonitrile has bound in the axial position, and that the MS contribution comes from both TMC and an axial acetonitrile. For direct comparison, an EXAFS fit was generated for $[Fe(IV)(TMC)(O)(CH_3CN)]^{2+}$ that was produced via an oxo-transfer reaction (Fit **OT**, Supplementary Table 8). Fit **3C** and **OT** are very similar, with only slight changes in the bond variances, illustrating that in the case of a known structure, the increased outer shell intensity of the FT is well fit with an axial acetonitrile.

**Fe K Pre-edge XAS of 1, 2, and 3.** The Fe K pre-edge intensities of **1** (acetone), **2** (acetone/$CF_3CH_2OH$), and **3** (acetone) are shown in Fig. 2b in the text and given in Supplementary Table 5. These data show an increase in intensity across the series, going from **1** (6-coordinate ferric-peroxo) to **2** (5-coordinate ferric-hydroperoxo) to **3** (6-coordinate low-spin Fe(IV)=O). In all three complexes, the edge shape is fairly consistent with a slight shift to higher energy for **3** indicative of a larger $Z_{eff}$ in the Fe(IV)=O. Most noticeable is the increase in pre-edge intensity from **1** to **2**. As **2** could not be isolated in acetonitrile as a result of the fast conversion of **1** to **3**, thus **3** in acetonitrile is believed to contain the least amount of contamination of **2**, resulting in a pre-edge intensity of ~37.2 units. This pre-edge intensity is greater than the ~30 units pre-edge intensity for $[Fe(IV)(TMC)(O)(CH_3CN)]^{2+}$ prepared via oxo-transfer reaction where the axial ligand and structural conformation are known by X-ray crystallography (*S3*). In addition, these data exhibit some differences in the XANES region, suggesting that **3** as a decay product of **1** and **2**, may have some structural differences in ring conformation and/or oxo-orientation (*syn*/*anti*) relative to $[Fe(IV)(TMC)(O)(CH_3CN)]^{2+}$ (*S21*).

**Acknowledgements**

The research was supported by NRF/MEST of Korea through the CRI (W.N.), GRL (2010-00353) (W.N.), WCU (R31-2008-000-10010-0) (W.N. and J.S.V.), the 2011 KRICT OASIS Project (W.N.), NIH Grants GM 40392 (E.I.S.), RR-001209 (K.O.H.), and National Science Foundation Grant MCB 0919027 (E.I.S.). J.J.B. acknowledges the fellowship from NSF EAPSI (OISE-1014685) and the Warner Linfield Award from the University of Michigan. Portions of this research were also carried out at the Stanford Synchrotron Radiation

Lightsource (SSRL), a Directorate of SLAC National Accelerator Laboratory and an Office of Science User Facility operated for the U.S. Department of Energy (DOE) Office of Science by Stanford University. The SSRL Structural Molecular Biology Program is supported by the Department of Energy, Office of Biological and Environmental Research, and by the NIH, National Center for Research Resources, Biomedical Technology Program. The publication was partially supported by Grant Number 5 P41 RR001209 from the National Center for Research Resources (NCRR), a component of the National Institutes of Health (NIH) and its contents are solely the responsibility of the authors and do not necessarily represent the official view of NCRR or NIH.

**References (Supplementary):**

S1. W. L. F. Armarego, D. D. Perrin, Eds. *Purification of Laboratory Chemicals* (Pergamon Press: Oxford, 1997).

S2. J. Annaraj, Y. Suh, M. S. Seo, S. O. Kim, W. Nam, *Chem. Commun.* **2005**, 4529 (2005).

S3. J.-U. Rohde *et al., Science* **299**, 1037 (2003).

S4. G. M. Sheldrick, SHELXTL/PC. Version 6.12 for Windows XP. 2001, Bruker AXS Inc., Madison, Wisconsin, USA.

S5. Source: SSRL Biological XAS beam line 9-3, 16-pole, 2-Tesla wiggler, 2.0 mrad beam, SPEAR3 at 3 GeV, 300 mA continuous fill. Optics: Si(220), liquid nitrogen cooled double crystal monochromator, fully tuned. Pre-monochromator flat, bent, harmonic rejection vertically collimating Rh coated Si M0 mirror; and post-monochromator bent, cylindrical, Rh coated Si focusing $M_1$ mirror; 10 keV cutoff,

energy resolution 1 x $10^{-4}$ ΔE/E.

S6. S. P. Cramer, O. Tench, M. Yochum, G. N. George, *Nucl. Instrum. Methods Phys. Rev.* **A266**, 586 (1988).

S7. R. A. Scott, J. E. Hahn, S. Doniach, H. C. Freeman, K. O. Hodgson, *J. Am. Chem. Soc.* **104**, 5364 **(**1982).

S8. S. P. Cramer, K. O. Hodgson, *Prog. Inorg. Chem.* **25**, 1 (1979).

S9. J. G. DeWitt *et al., J. Am. Chem. Soc.* **113**, 9219 (1991).

S10. R. A. Scott, *Methods Enzymol.* **177**, 414 (1985).

S11. A. Tenderholt, B. Hedman, K. O. Hodgson, *AIP Conference Proceedings* **882**, 105 (2007).

S12. G. N. George, EDG_FIT; Stanford Synchrotron Radiation Laboratory, Stanford Linear Acceleration Center, Stanford University, Stanford, CA 94309

S13. G. N. George, EXAFSPAK; Stanford Synchrotron Radiation Laboratory, Stanford Linear Acceleration Center, Stanford University, Stanford, CA 94309

S14. Gaussian 09, Revision B.01, M. J. Frisch, G. W. Trucks, H. B. Schlegel, G. E. Scuseria, M. A. Robb, J. R. Cheeseman, G. Scalmani, V. Barone, B. Mennucci, G. A. Petersson, H. Nakatsuji, M. Caricato, X. Li, H. P. Hratchian, A. F. Izmaylov, J. Bloino, G. Zheng, J. L. Sonnenberg, M. Hada, M. Ehara, K. Toyota, R. Fukuda, J. Hasegawa, M. Ishida, T. Nakajima, Y. Honda, O. Kitao, H. Nakai, T. Vreven, J. A. Montgomery, Jr., J. E. Peralta, F. Ogliaro, M. Bearpark, J. J. Heyd, E. Brothers, K. N. Kudin, V. N. Staroverov, R. Kobayashi, J. Normand, K. Raghavachari, A. Rendell, J. C. Burant, S. S. Iyengar, J. Tomasi, M. Cossi, N. Rega, J. M. Millam, M. Klene, J. E. Knox, J. B. Cross, V. Bakken, C. Adamo, J. Jaramillo, R. Gomperts, R. E. Stratmann, O. Yazyev,

A. J. Austin, R. Cammi, C. Pomelli, J. W. Ochterski, R. L. Martin, K. Morokuma, V. G. Zakrzewski, G. A. Voth, P. Salvador, J. J. Dannenberg, S. Dapprich, A. D. Daniels, Ö. Farkas, J. B. Foresman, J. V. Ortiz, J. Cioslowski, and D. J. Fox, Gaussian, Inc., Wallingford CT, 2009.

S15. F. Neese, E. I. Solomon, *J. Am. Chem. Soc.* **120**, 12829 (1998).

S16. J.-G. Liu, *et al. Angew. Chem. Int. Ed.* **48**, 9262 (2009).

S17. C. J. Cramer, W. B. Tolman, K. H. Theopold, A. L. Rheingold, *Proc. Natl Acad. Sci. USA* **100**, 3635 (2003).

S18. J.-U. Rohde *et al., J. Am. Chem. Soc.* **126**, 16750 (2004).

S19. M. R. Bukowski *et al., Science* **310**, 1000 (2005).

S20. M. H. Lim *et al., Proc. Natl. Acad. Sci. U.S.A.* **100**, 3665 (2003).

S21. K. Ray *et al. Angew. Chem. Int. Ed.* **47**, 8068 (2008).

**Supplementary Table 1**. Crystal data and structure refinements for **1**-($ClO_4$).

| | **1**-($ClO_4$) |
|---|---|
| Empirical formula | $C_{14}H_{32}ClFeN_4O_6$ |
| Formula weight | 443.74 |
| Temperature (K) | 200(2) |
| Wavelength (Å) | 0.71073 |
| Crystal system/space group | Monoclinic, *P2(1)* |
| Unit cell dimensions | |
| $a$ (Å) | 8.2773(14) |
| $b$ (Å) | 14.502(3) |
| $c$ (Å) | 8.7454(15) |
| $\alpha$ (°) | 90.00 |
| $\beta$ (°) | 110.833(9) |
| $\gamma$ (°) | 90.00 |
| Volume (Å$^3$) | 981.2(3) |
| Z | 2 |
| Calculated density (g/cm$^{-3}$) | 1.502 |
| Absorption coefficient (mm$^{-1}$) | 0.942 |
| Reflections collected | 8362 |
| Independent reflections [$R$(int)] | 3708 [0.0420] |
| Refinement method | Full-matrix, least-squares on $F^2$ |
| Data/restraints/parameters | 3708 /1/239 |
| Goodness-of-fit on $F^2$ | 1.084 |
| Final $R$ indices [$I > 2$sigma($I$)] | $R_1$ = 0.0597, $wR_2$ = 0.1541 |
| $R$ indices (all data) | $R_1$ = 0.0637, $wR_2$ = 0.1605 |

**Supplementary Table 2**. Selected bond distances (Å) and angles (º) for **1**-($ClO_4$).

| **Bond distances (Å)** | |
|---|---|
| Fe1-O1 | 1.906(4) |
| Fe1-O2 | 1.914(4) |
| Fe1-N1 | 2.192(4) |
| Fe1-N2 | 2.256(5) |
| Fe1-N3 | 2.180(5) |
| Fe1-N4 | 2.273(4) |
| O1-O2 | 1.463(6) |
| **Bond angles (º)** | |
| O1-Fe1-O2 | 45.03(17) |
| Fe1-O1-O2 | 67.8(2) |
| Fe1-O2-O1 | 67.2(2) |
| N1-Fe1-N2 | 90.01(18) |
| N1-Fe1-N3 | 159.78(17) |
| N1-Fe1-N4 | 81.78(17) |
| N2-Fe1-N3 | 82.44(19) |
| N2-Fe1-N4 | 132.96(16) |
| N3-Fe1-N4 | 89.67(17) |

**Supplementary Table 3**. First shell EXAFS fits to **1**, **2**, and **3**.

| Complex | Fit # | Path | CN | R(Å) | $\sigma^2$ (Å$^2$) | $\Delta E_0$ | Error |
|---|---|---|---|---|---|---|---|
| **1** | 1-1 | Fe-O | 1 | 1.92 | 86 | -0.2 | 1.05 |
| | | Fe-N | 5 | 2.23 | 582 | | |
| | 1-2 | Fe-O | 1 | 1.92 | 92 | -0.6 | 0.96 |
| | | Fe-N | 4 | 2.23 | 418 | | |
| | 1-3 | Fe-O | 2 | 1.92 | 352 | -3.2 | 0.83 |
| | | Fe-N | 4 | 2.22 | 409 | | |
| **2** | 2-1 | Fe-O | 2 | 1.89 | 2495 | -3.7 | 0.81 |
| | | Fe-N | 4 | 2.17 | 527 | | |
| | 2-2 | Fe-O | 1 | 1.85 | 526 | -1.5 | 0.72 |
| | | Fe-N | 4 | 2.17 | 584 | | |
| **3** | 3-1 | Fe-O | 1 | 1.66 | 520 | -3.9 | 0.71 |
| | | Fe-N | 4 | 2.08 | 395 | | |
| | 3-2 | Fe-O | 1 | 1.66 | 545 | -4.2 | 0.64 |
| | | Fe-N | 5 | 2.08 | 511 | | |

First shell EXAFS fits of complex **1**, **2**, and **3** ($k$ = 16 Å$^{-1}$) in acetone/$CF_3CH_2OH$. All distances are in Å. CN is coordination number. Bond variances ($\sigma^2$) are multiplied by $10^5$ for convenience. All paths are calculated as single scattering pathways. Errors in distance are ± 0.02 Å and coordination numbers are ± 25% as known from previous studies. Normalized error is given as $\chi^2$.

**Supplementary Table 4.** Final EXAFS Fits for **1**, **2**, and **3** in acetone, acetone/$CF_3CH_2OH$, and acetone, respectively.

| | **1** ($\Delta E_0$ = -5.1) | | | | **2** ($\Delta E_0$ = -3.5) | | | | **3** ($\Delta E_0$ = -3.9) | | |
|---|---|---|---|---|---|---|---|---|---|---|---|
| | CN | R(Å) | $\sigma^2$ (Å$^2$) | | CN | R(Å) | $\sigma^2$ (Å$^2$) | | CN | R(Å) | $\sigma^2$ (Å$^2$) |
| Fe-OO | 2 | 1.92 | 303 | Fe-OOH | 1 | 1.85 | 661 | Fe=O | 1 | 1.67 | 556 |
| Fe-N | 4 | 2.21 | 420 | Fe-N | 4 | 2.16 | 534 | Fe-N | 5 | 2.08 | 539 |
| Fe-C | 8 | 3.01 | 812 | Fe-C | 8 | 2.97 | 885 | Fe-C | 8 | 2.96 | 1184 |
| TMC MS | 24 | 3.36 | 219 | TMC MS | 24 | 3.32 | 188 | TMC MS | 24 | 3.28 | 534 |
| Fe-C | 6 | 3.59 | 1289 | Fe-C | 6 | 3.57 | 1943 | Fe-C | 6 | 3.36 | 4125 |
| Error | | | 0.201 | | | | 0.189 | | | | 0.303 |

All distances are in Å. CN is coordination number. Bond variances ($\sigma^2$) are multiplied by $10^5$ for convenience. All paths are calculated as single scattering pathways, unless otherwise noted (multiple scattering paths is MS). Errors in distance are ± 0.02 Å and coordination numbers are ± 25%. Normalized error is given as $\chi^2$.

**Supplementary Table 5.** Fe K pre-edge energy and intensity fit values for **1**, **2**, and **3.**

| | Peak 1 (eV) | Area | Peak 2 (eV) | Area | Total Intensity |
|---|---|---|---|---|---|
| $[Fe(III)(TMC)(OO)]^{+}$ (**1**) | 7112.7 | 11.9 | 7114.4 | 5.6 | 17.5 ± 1.9 |
| $[Fe(III)(TMC)(OOH)]^{2+}$ (**2**) | 7112.9 | 19.0 | 7114.3 | 6.6 | 25.6 ± 2.3 |
| $Fe(IV)(TMC)(O)]^{2+}$ (**3**) | 7113.1 | 23.9 | 7114.2 | 7.0 | 30.9 ± 2.1 |
| $[Fe(IV)(TMC)(O)]^{2+}$ (**3**) **(**Acetonitrile) | 7113.0 | 28.8 | 7114.0 | 8.4 | 37.2 ± 2.0 |
| $[Fe(IV)(TMC)(O)(CH_3CN)]^{2+}$ | 7112.9 | 23.0 | 7113.9 | 7.0 | 30.0 ± 1.1 |

Fe K pre-edge fits for **1**, **2**, and **3** in acetone, acetone/$CF_3CH_2OH$, and acetone, respectively. Pre-edge intensities for **3** in acetonitrile as well as $[Fe(IV)(TMC)(O)(CH_3CN)]^{2+}$ prepared by oxo-transfer from $[Fe(II)(TMC)]^{2+}$ are also included for reference. Peak energies are listed at maximum, areas are multiplied by 100 for comparison to previously published data. Total intensity is the sum of both areas. Error values are calculated from total intensity standard deviations from nine separate fits.

**Supplementary Table 6**. Kinetic data obtained in the conversion of **2** (1 mM) to **3** performed with different amounts of $HClO_4$.

| | | Amount of $HClO_4$, $k_{obs}$ / $s^{-1}$ | | |
|---|---|---|---|---|
| Solvent | Temperature | 3 mM | 30 mM | 100 mM |
| $CH_3CN$ | -40 °C | $2.3(2) \times 10^{-2}$ | $2.7(3) \times 10^{-1}$ | 1.6(2) |
| Acetone:$CF_3CH_2OH$ (3:1) | -20 °C | $4.3(3) \times 10^{-3}$ | $4.5(3) \times 10^{-3}$ | $4.5(3) \times 10^{-3}$ |
| Acetone | -20 °C | $2.7(2) \times 10^{-3}$ | $2.9(2) \times 10^{-3}$ | $2.8(2) \times 10^{-3}$ |
| $CF_3CH_2OH$ | -20 °C | $4.4(3) \times 10^{-3}$ | $6.1(4) \times 10^{-3}$ | $6.6(4) \times 10^{-3}$ |

It should be noted that the rates of formation of **3** varied significantly depending on the solvent system.

**Supplementary Table 7.** Solvent dependent final EXAFS fits for $[Fe(IV)(TMC)(O)]^{2+}$ (**3**).

| | **3A** ($\Delta E_0$ = -2.9) | | | | **3B** ($\Delta E_0$ = -3.5) | | | | **3C** ($\Delta E_0$ = -3.9) | | |
|---|---|---|---|---|---|---|---|---|---|---|---|
| | CN | R(Å) | $\sigma^2$ (Å$^2$) | | CN | R(Å) | $\sigma^2$ (Å$^2$) | | CN | R(Å) | $\sigma^2$ (Å$^2$) |
| Fe=O | 1 | 1.66 | 483 | Fe=O | 1 | 1.67 | 754 | Fe=O | 1 | 1.67 | 819 |
| Fe-N | 5 | 2.09 | 532 | Fe-N | 5 | 2.10 | 526 | Fe-N | 5 | 2.10 | 519 |
| Fe-C | 8 | 2.97 | 1338 | Fe-C | 8 | 2.95 | 1235 | Fe-C | 8 | 3.02 | 1125 |
| TMC MS | 24 | 3.28 | 798 | TMC MS | 24 | 3.20 | 106 | $CH_3CN$ MS | 2 | 3.25 | 134 |
| Fe-C | 6 | 3.38 | 4670 | Fe-C | 6 | 3.61 | 982 | Fe-C | 6 | 3.55 | 1303 |
| Error | | | 0.128 | | | | 0.300 | | | | 0.345 |

Final EXAFS Fits for $[Fe(IV)(TMC)(O)]^{2+}$ complexes, **3A** (acetone) and **3B/C** (acetonitrile). All data (k=12 Å$^{-1}$, Supplementary Fig. 23) were fit using the same number and set of single scattering paths. **3A** and **3B** were fit using TMC for the multiple scattering (MS) contribution, whereas **3C** includes the forward focused acetonitrile MS path. All distances are in Å. CN is coordination number. Bond variances ($\sigma^2$) are multiplied by $10^5$. All paths are calculated as single scattering pathways unless otherwise noted (MS). Errors in distance are ± 0.02 Å and coordination numbers are ± 25%. Normalized error is given as $\chi^2$.

**Supplementary Table 8.** Comparative EXAFS fit to $[Fe(IV)(TMC)(O)(CH_3CN)]^{2+}$.

| | **3C** ($\Delta E_0$ = -3.9) | | | | **OT** ($\Delta E_0$ = -4.1) | | |
|---|---|---|---|---|---|---|---|
| | CN | R(Å) | $\sigma^2$ (Å$^2$) | | CN | R(Å) | $\sigma^2$ (Å$^2$) |
| Fe-O | 1 | 1.67 | 819 | Fe-O | 1 | 1.66 | 559 |
| Fe-N | 5 | 2.10 | 519 | Fe-N | 5 | 2.08 | 525 |
| Fe-C | 8 | 3.02 | 1125 | Fe-C | 8 | 3.01 | 1324 |
| $CH_3CN$ MS | 2 | 3.25 | 134 | $CH_3CN$ MS | 2 | 3.20 | 483 |
| Fe-C | 6 | 3.55 | 1303 | Fe-C | 6 | 3.46 | 1484 |
| Error | | | 0.345 | | | | 0.142 |

EXAFS fits to $[Fe(IV)(TMC)(O)(CH_3CN)]^{2+}$ prepared via an oxo-transfer (OT) reaction for compared with **3** in acetonitrile (**3C** Supplementary Fig. 23). Fit **3C,** is reproduced from Supplementary Table 7. All distances are in Å. CN is coordination number. Bond variances ($\sigma^2$) are multiplied by $10^5$ for convenience. All paths are calculated as single scattering pathways unless otherwise noted (MS). Errors in distance are ± 0.02 Å and coordination numbers are ± 25%. Normalized error is given as $\chi^2$.

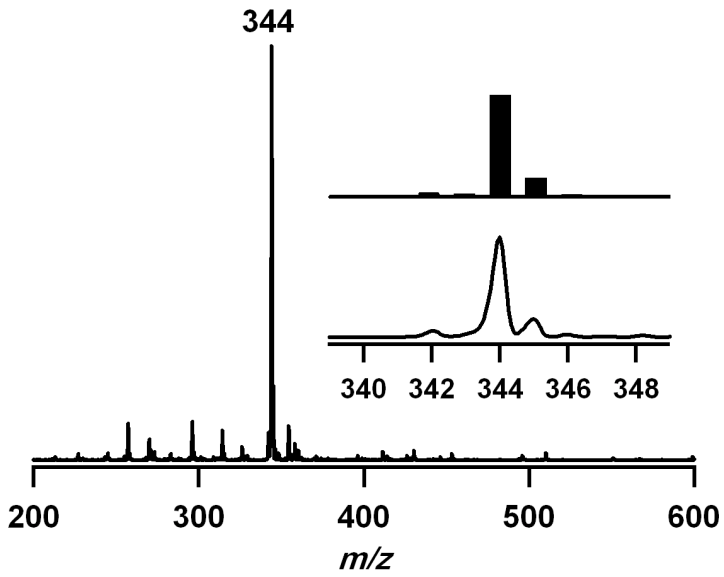


**Supplementary Figure 1.** ESI MS of $[Fe(III)(TMC)(OO)]^+$ (**1**) prepared in $CF_3CH_2OH$ at –20 °C. Insets are the experimental (lower) and simulated (upper) spectra of **1** in the region of *m/z* 339 – 349. The ion peak at *m*/*z* = 344 corresponds to $[Fe(III)(TMC)(OO)]^+$.

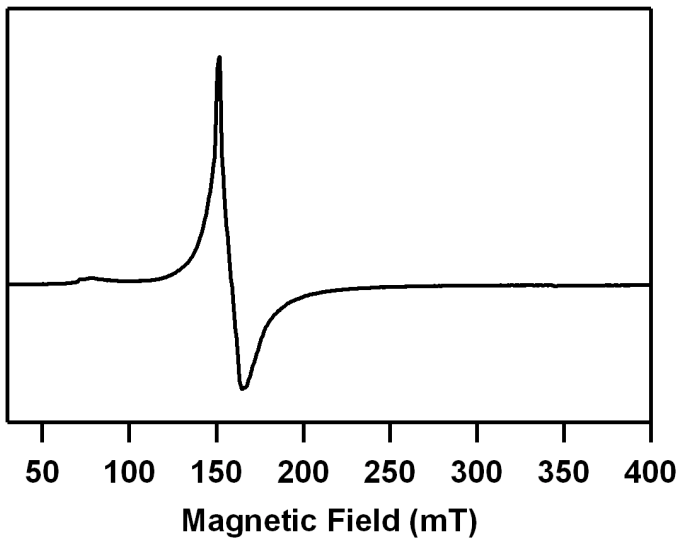


**Supplementary Figure 2.** X-band EPR spectrum of $[Fe(III)(TMC)(OO)]^{+}$ (**1**) (*g* values = 5.9 and 4.3) in frozen $CH_3CN$ at 4.3 K. Instrumental parameters: microwave power = 0.999 mW, frequency = 9.6 GHz, sweep width = 0.5 T, modulation amplitude = 1 mT.

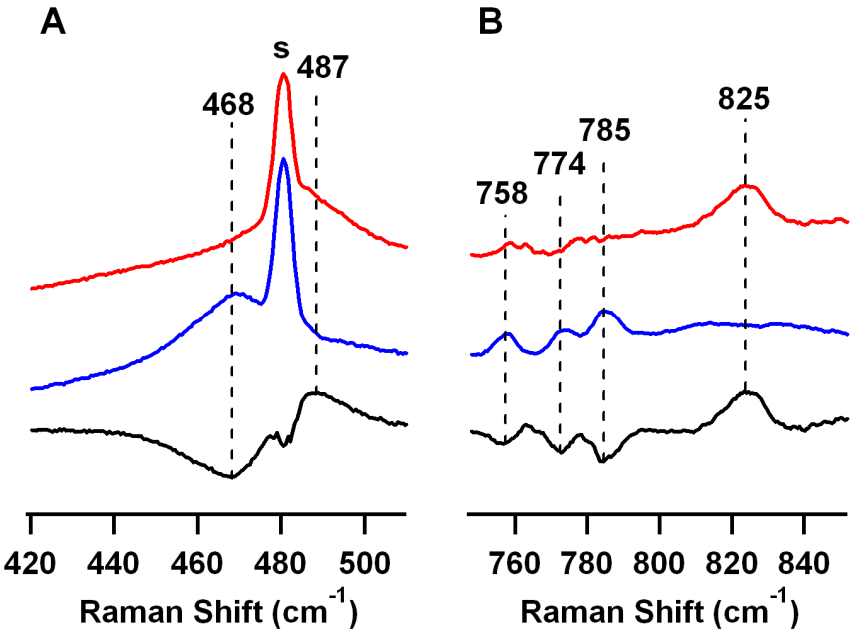


**Supplementary Figure 3.** Resonance Raman spectra of $[Fe(III)(TMC)(OO)]^{+}$ (**1**) in $d_6$-acetone with $^{16}O$ (red) and $^{18}O$ (blue) isotopic substitution in the region of Fe-O and O-O stretches ($\lambda_{ex}$ = 778 nm, 300 mW power, 77 K). Black is the $^{16}O$ and $^{18}O$ difference. The peak marked with "s" is ascribed to the solvent. Note from DFT studies, the isotope independent band at 758 $cm^{-1}$ can be assigned to an Fe-N symmetric stretch of the TMC chelate.

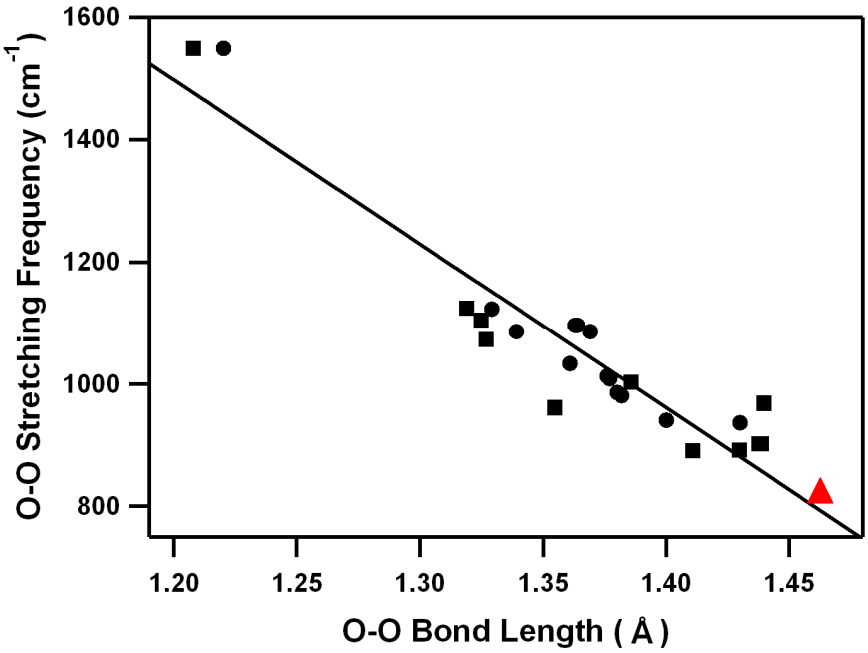


**Supplementary Figure 4.** Plot of the O-O stretching frequency ($cm^{-1}$) vs the O-O bond distance (Å) for side-on metal-OO complexes. Squares represent experimental data points, and circles represent theoretical ones taken from C. J. Cramer, W. B. Tolman, K. H. Theopold, A. L. Rheingold, *Proc. Natl. Acad. Sci. U.S.A.* **100**, 3635 (2003) and J. Cho, R. Sarangi, H. Y. Kang, J. Y. Lee, M. Kubo, T. Ogura, E. I. Solomon, W. Nam, *J. Am. Chem. Soc*. **132**, 16977 (2010). The solid line represents a least-squares linear fit of the experimental and theoretical data. Data point for $[Fe(III)(TMC)(OO)]^+$ (**1**) (▲) is included in the diagram.

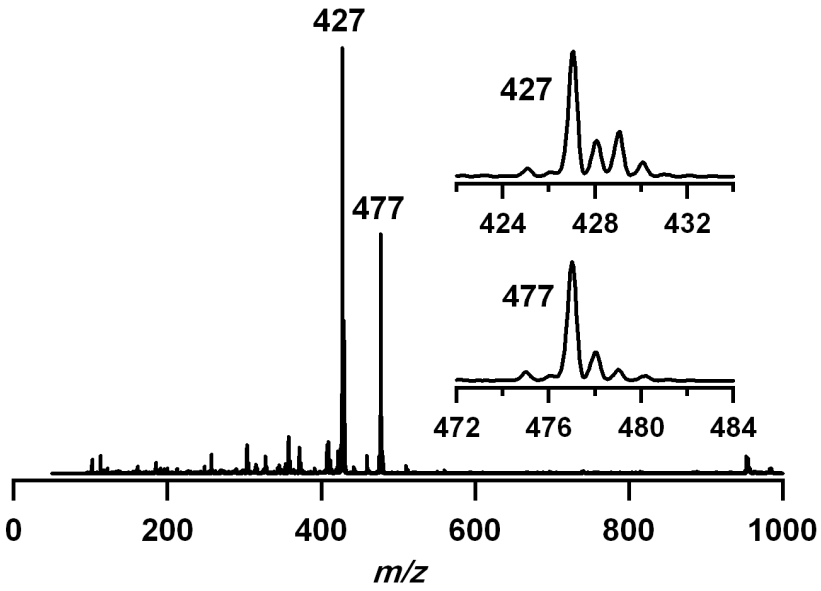


**Supplementary Figure 5.** ESI MS of $[Fe(IV)(TMC)(O)]^{2+}$ (**3**) produced in the conversion of $[Fe(III)(TMC)(OOH)]^{2+}$ (**2**) in acetone at 0 °C. The ion peaks at *m*/*z* = 427 and 477 correspond to $\{[Fe(IV)(TMC)(O)](ClO_4)\}^+$ and $\{[Fe(IV)(TMC)(O)](CF_3SO_3)\}^+$, respectively.

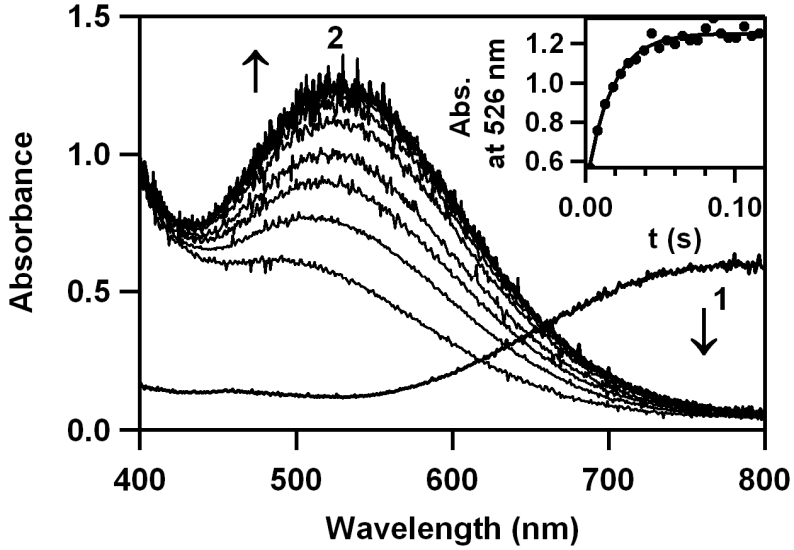


**Supplementary Figure 6.** UV-vis (stopped-flow) spectral changes observed in the reaction of **1** (1 mM) with 3 equiv $HClO_4$ in acetone/$CF_3CH_2OH$ (3:1) at –40 °C. Inset shows the time course of the absorbance at 526 nm ($k_{obs}$ = 93 $s^{-1}$). Arrows indicate spectral changes for the immediate conversion of **1** to **2'** and the gradual formation of **2**. The rate of formation of **2** from **1** was not dependent on proton concentration in acetone/$CF_3CH_2OH$ (3:1).

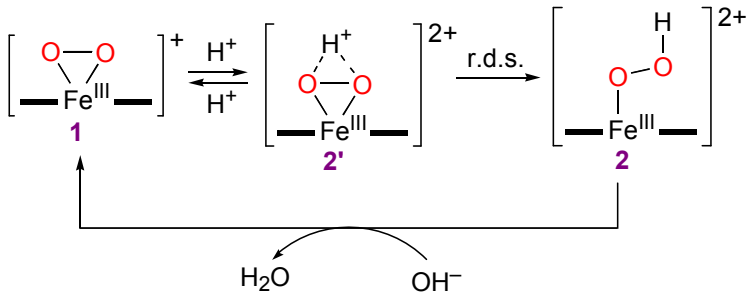


**Supplementary Figure 7.** Reaction pathways showing the conversion of **1** to **2** via the short-lived intermediate **2'** upon addition of proton to **1** and the conversion of **2** to **1** upon addition of hydroxide to **2**. See Supplementary Figs. 6 and 8 for electronic absorption spectral changes. We should mention here that besides the electronic absorption spectrum, there is no clear spectroscopic evidence for the structure of **2'** as a side-on iron(III)-hydroperoxo species.

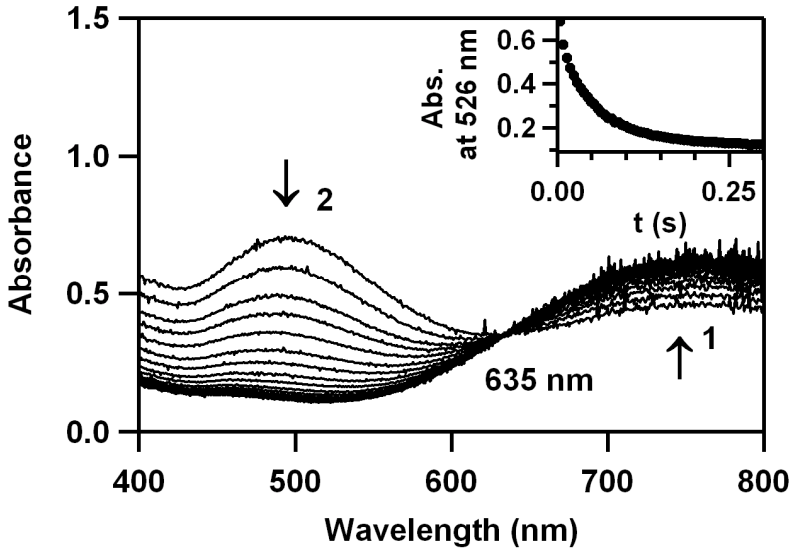


**Supplementary Figure 8.** UV-vis (stopped-flow) spectra of **2** with 3 equiv TMAH in acetone/$CF_3CH_2OH$ (3:1) at –80 °C. Inset shows the time course of the absorbance at 526 nm ($k_{obs}$ = 19 $s^{-1}$). Arrows indicate spectral changes for the conversion of **2** to **1** with an isosbestic point at 635 nm.

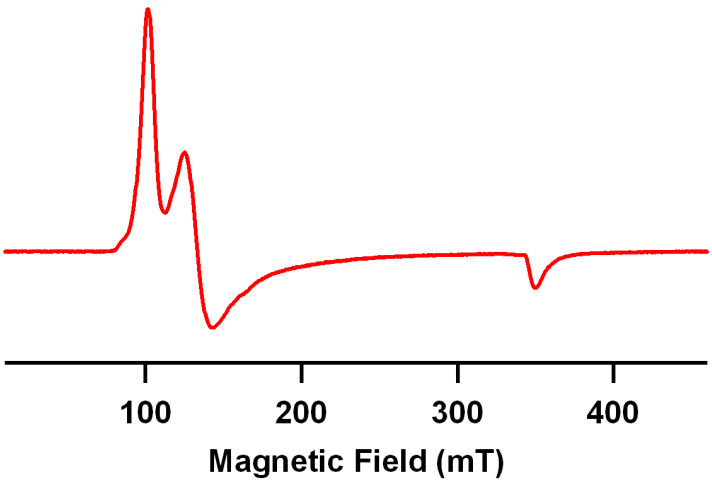


**Supplementary Figure 9.** X-band EPR spectrum of **2** (1 mM) in frozen acetone/$CF_3CH_2OH$ (3:1) at 10 K. Instrumental parameters: microwave power = 1.055 mW, frequency = 9.6 GHz, sweep width = 0.45 T, modulation amplitude = 1 mT.

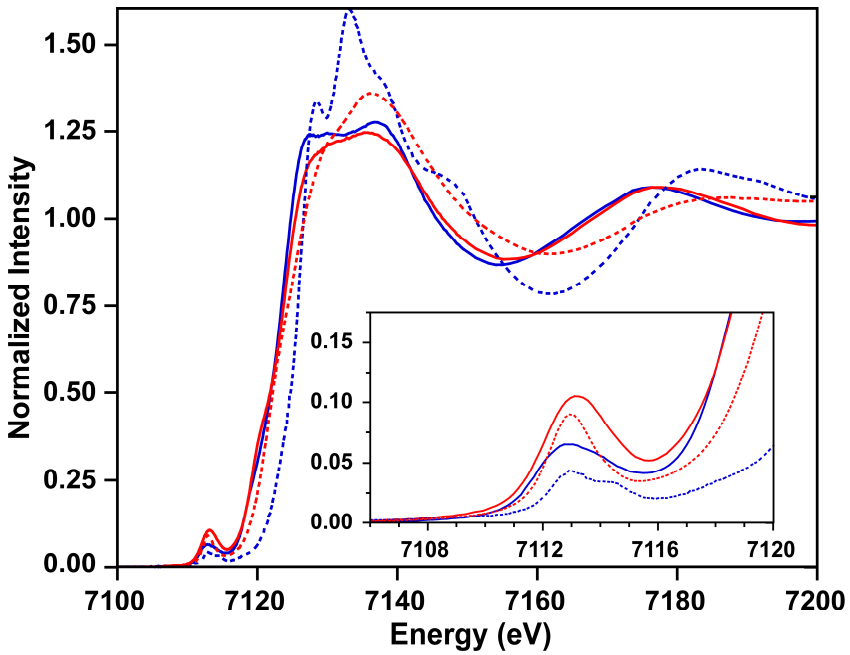


**Supplementary Figure 10.** Fe K-edge and pre-edge (inset) of $[Fe(III)(TMC)(OOH)]^{2+}$ (**2**) (— red) (acetone/$CF_3CH_2OH$) and $[Fe(III)(TMC)(OO)]^{+}$ (**1**) (— blue) (acetone) compared with $K_3[Fe(III)(oxalate)_3]$ (---- blue) (6-coordinate $O_h$) and Fe(salen)Cl (----- red) (5-coordinate $C_{4v}$) complexes. From comparison to the models, **2** has a 5-coordinate high-spin Fe(III) site.

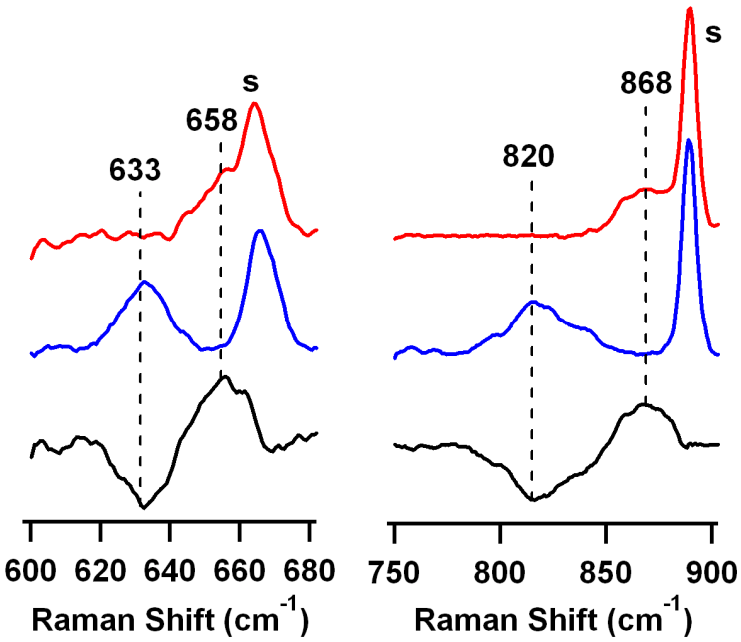


**Supplementary Figure 11.** Resonance Raman spectra of **2** in $d_6$-acetone with $^{16}O$ (red) and $^{18}O$ (blue) isotopic substitution in the region of Fe-O and O-O stretches ($\lambda_{ex}$ = 531-nm, 60 mW power, 77 K). Black is the $^{16}O$ and $^{18}O$ difference. The peaks marked with "s" are from the solvent.

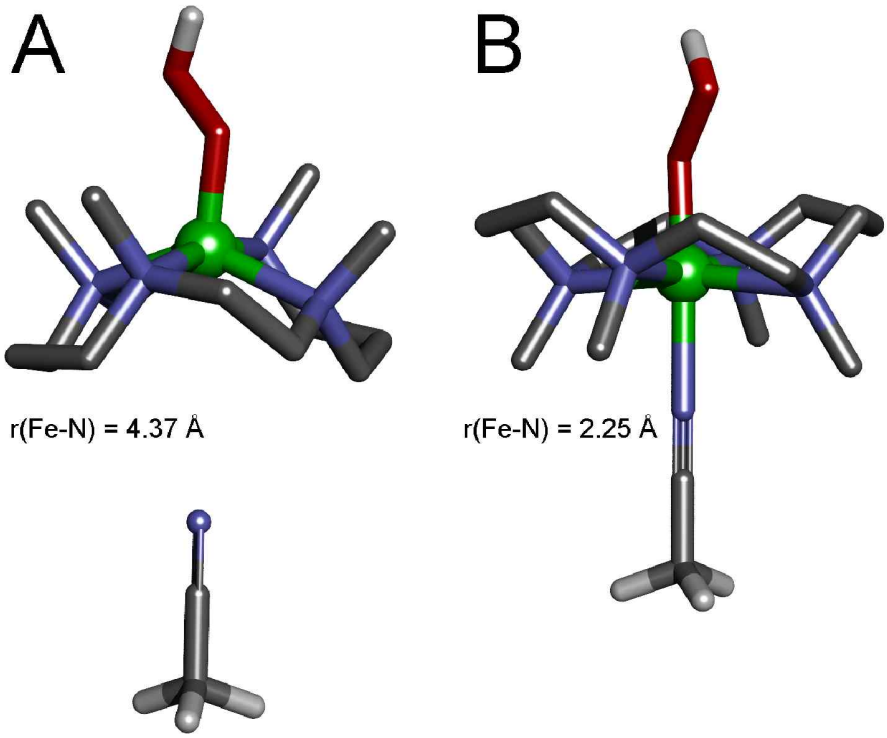


**Supplementary Figure 12.** (**A**) DFT optimized structure of $[Fe(III)(TMC)(OOH)]^{2+}$ (**2**) with its methyl groups *syn* to the $OOH^-$ and *anti* to acetonitrile. (**B**) DFT optimized structure of **2** with its methyl groups *anti* to the $OOH^-$ and *syn* to acetonitrile. **B** is 6 kcal/mol higher in energy than **A**.

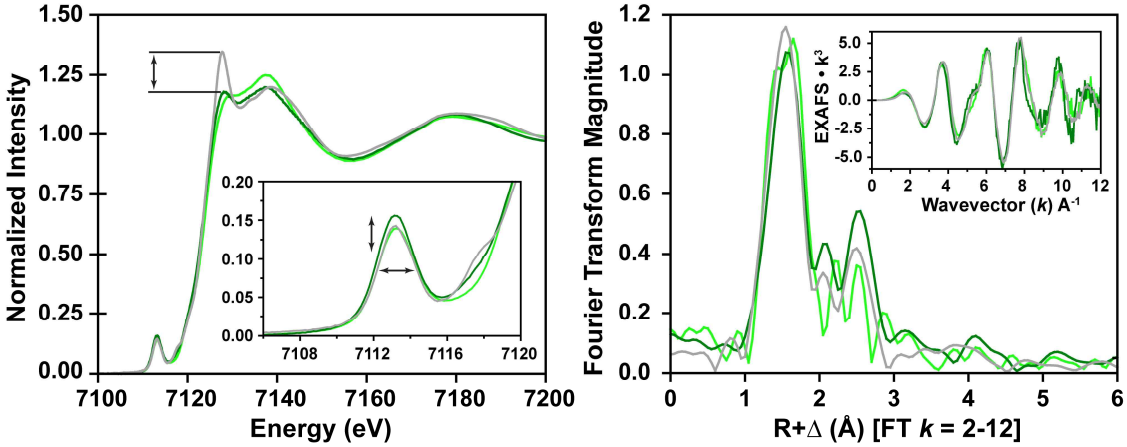


**Supplementary Figure 13.** XAS edge and EXAFS data of $[Fe(IV)(TMC)(O)]^{2+}$ (**3**) in acetone (light green) and acetonitrile (dark green) vs. $[Fe(IV)(TMC)(O)(CH_3CN)]^{2+}$ (grey) prepared from $[Fe(II)(TMC)]^{2+}$ using an oxo-transfer (OT) reagent. Left: Fe K-edge and K pre-edge. The pre-edge exhibits an intensity increase for **3** in acetonitrile relative to $[Fe(IV)(TMC)(O)(CH_3CN)]^{2+}$ (from ~30.0 to ~37.2) units as well as a diminished XANES signature at 7129 eV. This difference was observed for all decay products **3**, regardless of solvent. In the case of **3** (acetone), the less intense pre-edge (~30.9 units) may be due to incomplete conversion to the Fe(IV)=O end product. Right: Fourier transform and EXAFS (inset). Data quality of **3** in acetonitrile limited the EXAFS data to $k$ = 12 $Å^{-1}$, and thus all data sets were truncated for accurate comparison across the series. All exhibit a similar EXAFS pattern, however, **3** shows a substantial increase in the outer shell intensity at R+Δ = ~2.25 Å for acetonitrile vs. acetone. This increase can be accounted for in the EXAFS data by an intense forward focused MS pathway from the placement of an axial acetonitrile (see fits in Supplementary Table 7).

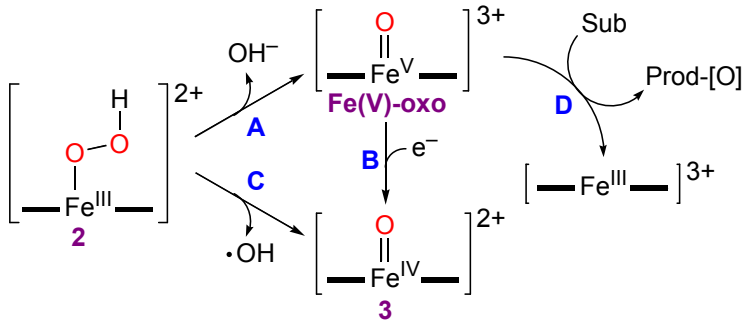


**Supplementary Figure 14.** Possible mechanisms for the formation of **3** from **2** via O-O bond heterolysis (pathway A) and homolysis (pathway C). We did not observe the formation of $[Fe(III)(TMC)]^{3+}$ (i.e., pathways A and D) when protons were added to a solution of **1** (1 mM) containing substrates (10 mM – 100 mM), such as ethylbenzene, cyclohexene, cyclohexadiene, and thioanisole, in $CH_3CN$ at –40 °C. Instead, we observed the formation of **3** in these reactions, suggesting that the formation of **3** occurs via pathway of **C**, not pathways **A** and **B**.

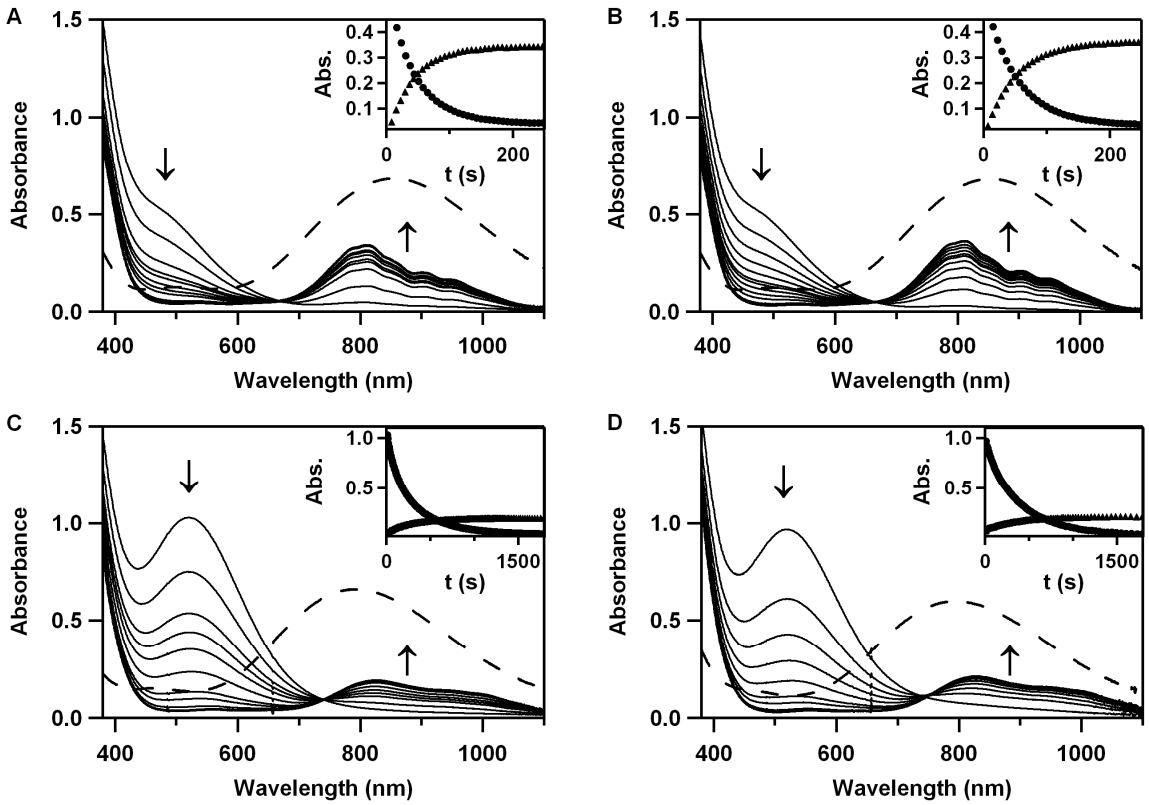


**Supplementary Figure 15.** Formation of $[Fe(IV)(TMC)(O)]^{2+}$ (**3**) upon addition of 3 equiv $HClO_4$ to the solution of $[Fe(III)(TMC)(OO)]^{+}$ (**1**) in the absence and presence of 50 equiv cyclohexene. (**A**) Reaction was carried out in the absence of cyclohexene in $CH_3CN$ at –40 °C. (**B**) Reaction was carried out in the presence of cyclohexene in $CH_3CN$ at –40 °C. (**C**) Reaction was carried out in the absence of cyclohexene in acetone/$CF_3CH_2OH$ (3:1) at –20 °C. (**D**) Reaction was carried out in the presence of cyclohexene in acetone/$CF_3CH_2OH$ (3:1) at –20 °C. The amounts of **3** formed in the absence and presence of cyclohexene (and other substrates mentioned in the text) were the same in those reactions. Insets show the time course of the absorbance at 526 (●) and 823 (▲) nm. No substrate effect was observed when other substrates, such as ethylbenzene, cyclohexadiene, and thioanisole, were used.

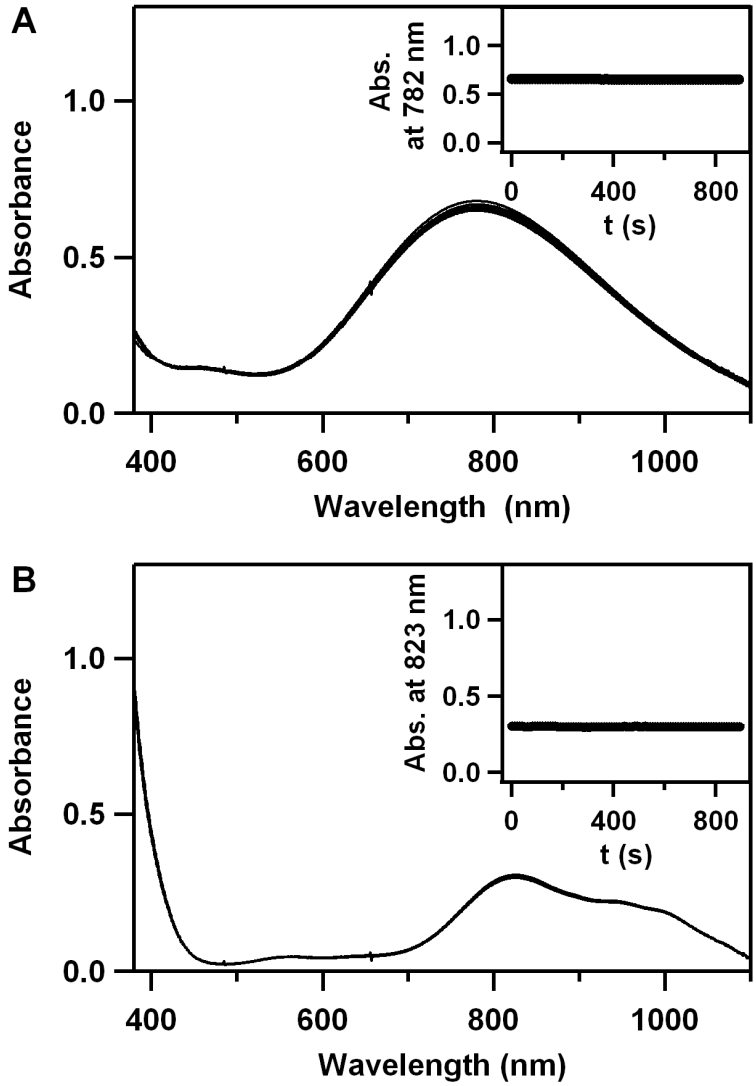


**Supplementary Figure 16.** Reactions of $[Fe(III)(TMC)(OO)]^{+}$ (**1**) and $[Fe(IV)(TMC)(O)]^{2+}$ (**3**) with 2-phenylpropionaldehyde (2-PPA) in acetone/$CF_3CH_2OH$ (3:1) at –40 °C. (**A**) UV-vis spectral changes of **1** (1 mM) upon addition of 50 equiv of 2-PPA. Inset shows the time course of the absorbance at 782 nm. (**B**) UV-vis spectral changes of **3** (1 mM) upon addition of 50 equiv of 2-PPA in the presence of 3 equiv of $HClO_4$. Inset shows the time course of the absorbance at 823 nm.

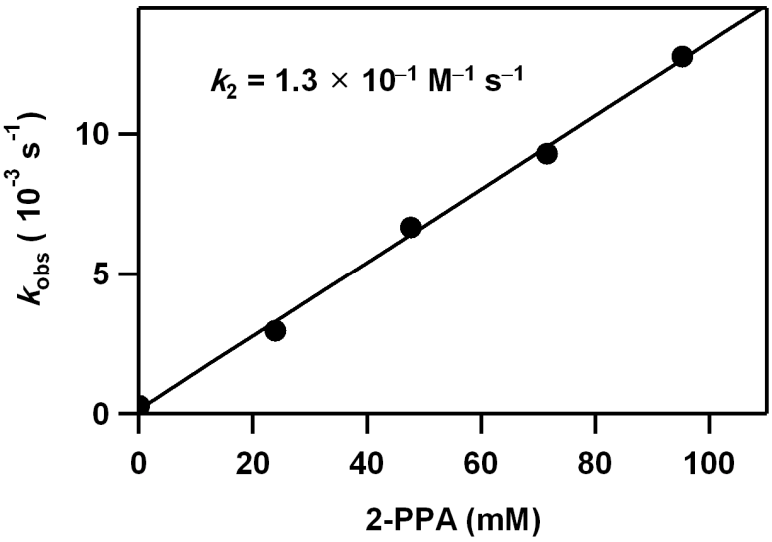


**Supplementary Figure 17.** Reaction of $[Fe(III)(TMC)(OOH)]^{2+}$ (**2**) with 2-phenylpropionaldehyde (2-PPA). Plot of $k_{obs}$ against 2-PPA concentration to determine a second-order rate constant. Standard deviation is <10% of the data used in drawing the plot. Product analysis of the reaction solution revealed the formation of acetophenone (90 ± 10% based on **2**). The formation of **3** was observed in the reaction of **2** and 2-PPA owing to the low reactivity of **3** with aldehydes, as discussed in text. Detailed mechanistic studies are underway in this laboratory to understand the mechanism of the formation of **3** in the reaction of **2** and 2-PPA.

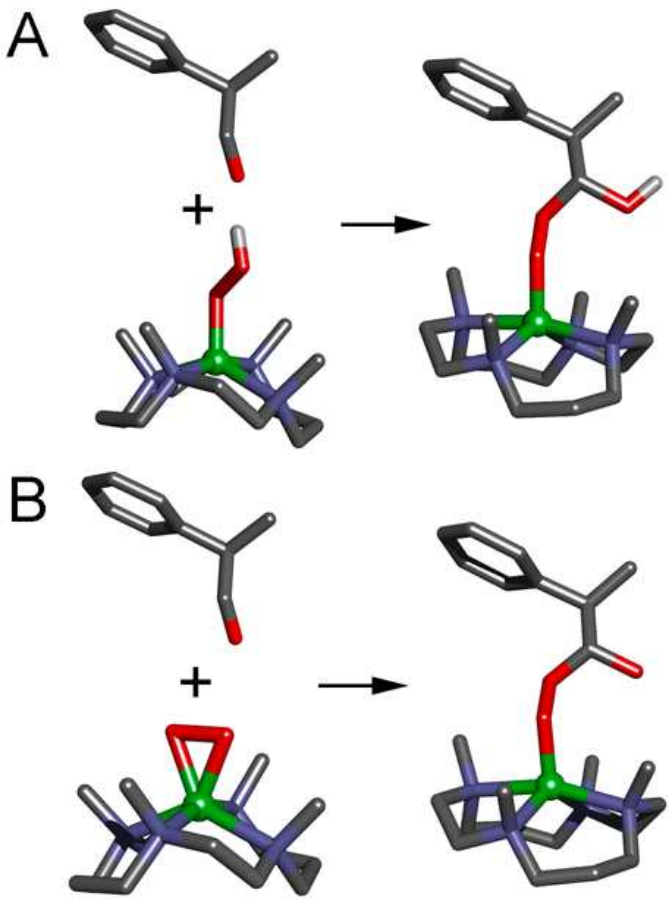


**Supplementary Figure 18.** (A) DFT studies show that $[Fe(III)(TMC)(OOH)]^{2+}$ reacts with 2-phenylpropionaldehyde (2-PPA) to protonate the carbonyl and form a peroxo bridge to its carbon. The ΔG(PCM) for this reaction is –1.4 kcal/mol. (B) For the side-on Fe(III)-peroxo, the energy to form a peroxo bridge to the carbonyl carbon is ΔG(PCM) of 23.6 kcal/mol. Therefore, our calculations strongly support our experimental observation that the end-on Fe(III)-hydroperoxo is more active than the side-on Fe(III)-peroxo in nucleophilic reactions.

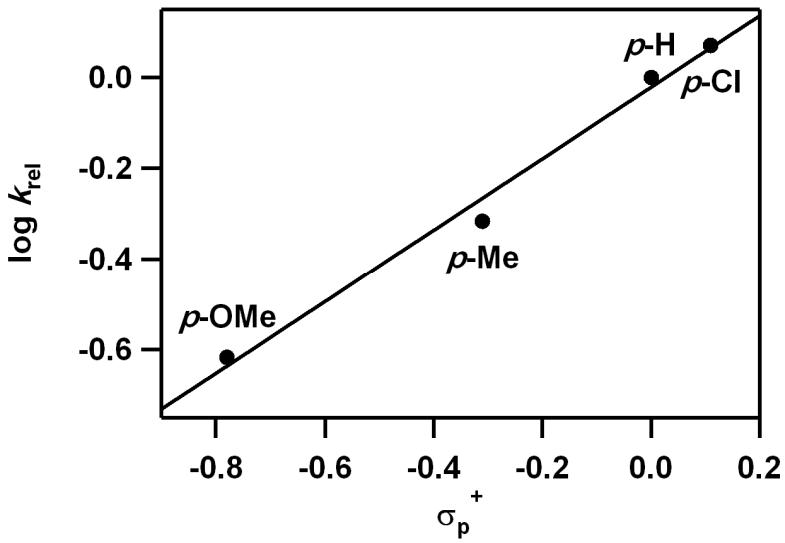


**Supplementary Figure 19.** Hammett plot of log $k_{rel}$ against $\sigma_p^+$ of *para*-substituted benzaldehydes, *para*-Y-Ph-CHO (Y = OMe, Me, H, Cl), by $[Fe(III)(TMC)(OOH)]^{2+}$ (**2**). The $k_{rel}$ values were calculated by dividing $k_{obs}$ of *para*-substituted benzaldehydes by $k_{obs}$ of benzaldehyde. Standard deviation is <15% of the data used in drawing the plot. A positive $\rho^+$ value of 0.9 in the Hammett plot was obtained that is consistent with the process involving nucleophilic character of the Fe(III)-OOH unit in the oxidation of aldehydes.

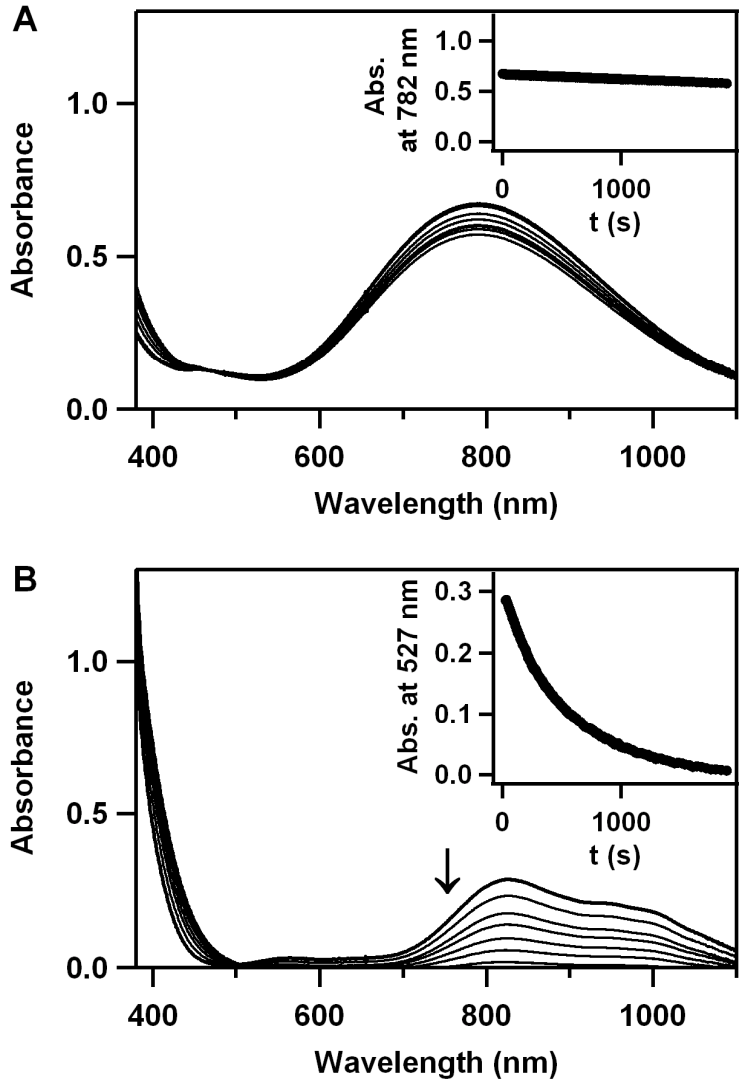


**Supplementary Figure 20.** Reactions of $[Fe(III)(TMC)(OO)]^{+}$ (**1**) and $[Fe(IV)(TMC)(O)]^{2+}$ (**3**) with 9,10-dihydroanthracene (DHA) in acetone/$CF_3CH_2OH$ (3:1) at –20 °C. (**A**) UV-vis spectral changes of **1** (1 mM) upon addition of 10 equiv of DHA. Inset shows the time course of the absorbance at 782 nm. (**B**) UV-vis spectral changes of **3** (1 mM) upon addition of 10 equiv of DHA in the presence of 3 equiv of $HClO_4$. Inset shows the time course of the absorbance at 823 nm.

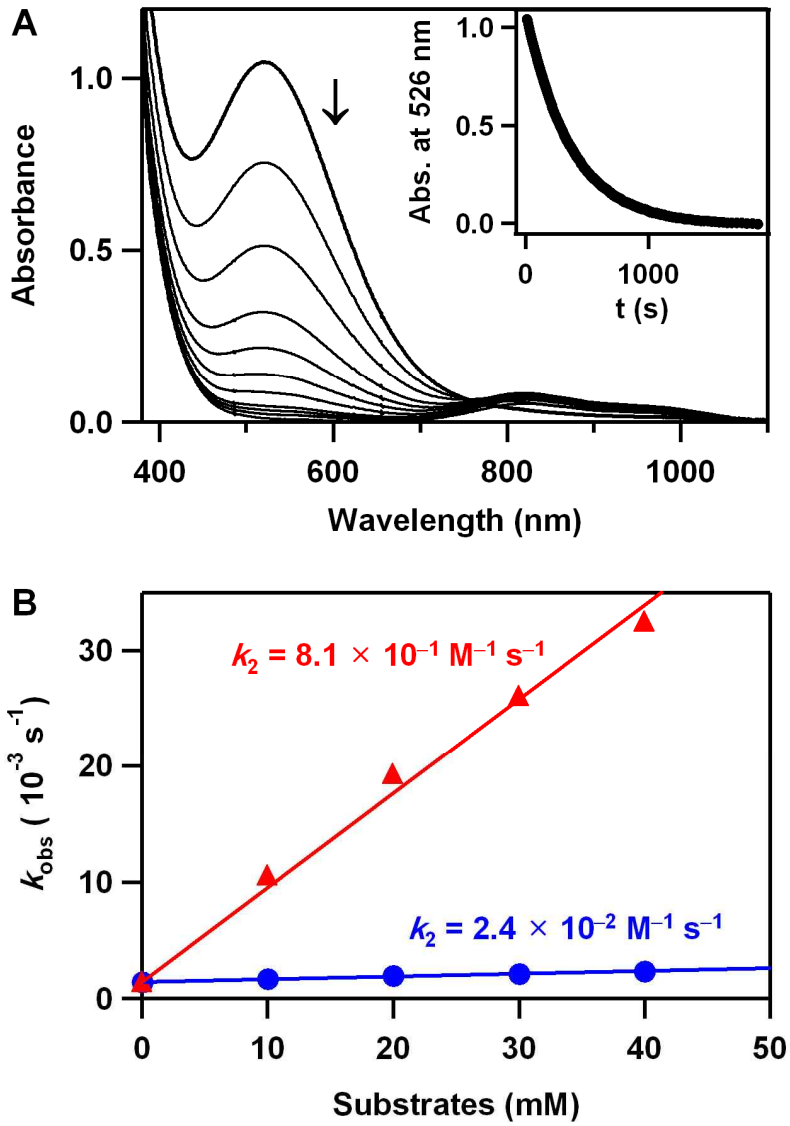


**Supplementary Figure 21.** Reaction of $[Fe(III)(TMC)(OOH)]^{2+}$ (**2**) with 9,10-dihydroanthracene (DHA) in acetone/$CF_3CH_2OH$ (3:1) at –20 °C. (**A**) UV-vis spectral changes of **2** (1 mM) upon addition of 10 equiv of DHA. Inset shows the time course of the absorbance at 526 nm. (**B**) Plots of $k_{obs}$ against concentrations of DHA (●) and xanthene (▲) to determine second-order rate constants. Standard deviation is <10% of the data used

in drawing the plot. Product analysis of the reaction solutions revealed that xanthone and anthracene were produced with high yields (85 ± 10%) in the oxidation of xanthene and DHA, respectively, as observed in other nonheme iron(IV)-oxo complex-mediated oxidation reactions: (a) Yiu, D. T. Y. *et al.*, *Inorg. Chem*. **42**, 1225 (2003). (b) Lansky, D. E. & Goldberg, D. P., *Inorg. Chem*. **45**, 5119 (2006). (c) Sastri, C. V. *et al.*, *Proc. Natl Acad. Sci. USA* **104**, 19181 (2007).

Similar reactivities observed in the reactions of the iron(III)-hydroperoxo complex, $[Fe(III)(TMC)(OOH)]^{2+}$, and the iron(IV)-oxo complex, $[Fe(IV)(TMC)(O)]^{2+}$, are ascribed to a larger steric effect of the TMC ligand in limiting access to Fe(IV)=O relative to the Fe(III)-OOH species: (a) Rohde, J.-U. *et al.*, *Science* **299**, 1037 (2003). (b) Wong, S. D. *et al.*, *Angew. Chem. Int. Ed.* **50**, 3215 (2011).

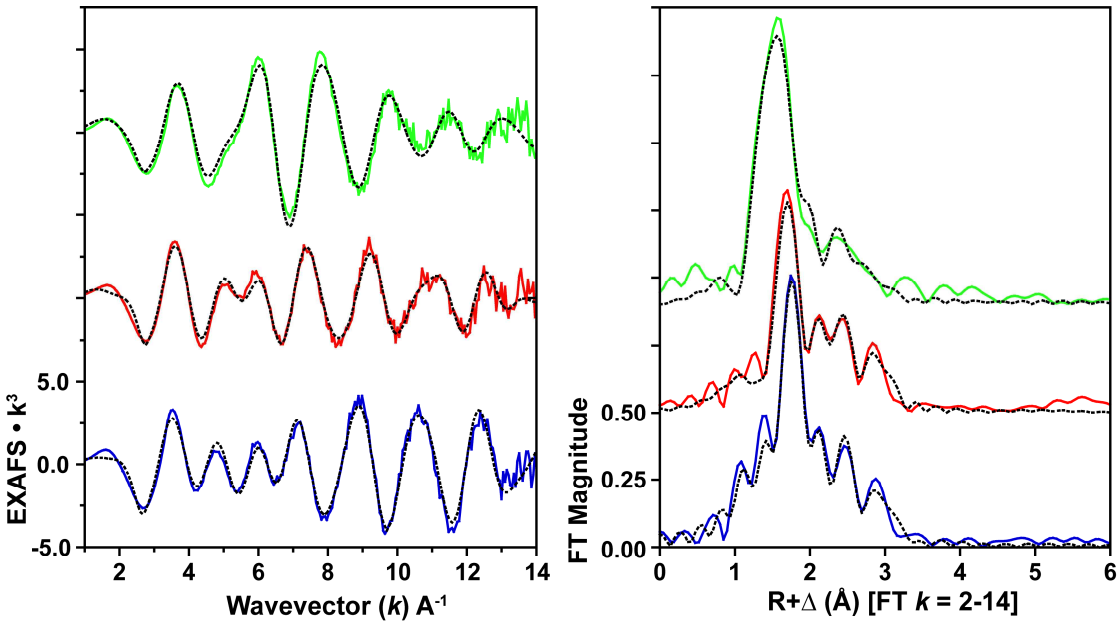


**Supplementary Figure 22**. EXAFS data (left) with their Fourier transform (right) for $[Fe(III)(TMC)(OO)]^{+}$ (**1**) (blue), $[Fe(III)(TMC)(OOH)]^{2+}$ (**2**) (red), and $[Fe(IV)(TMC)(O)]^{2+}$ (**3**) (green), data (—) and fits (----). Fit lines are for final EXAFS fits presented in Supplementary Table 4. The data quality of **1** limited the EXAFS fits to $k$ = 14 $Å^{-1}$ across the series.

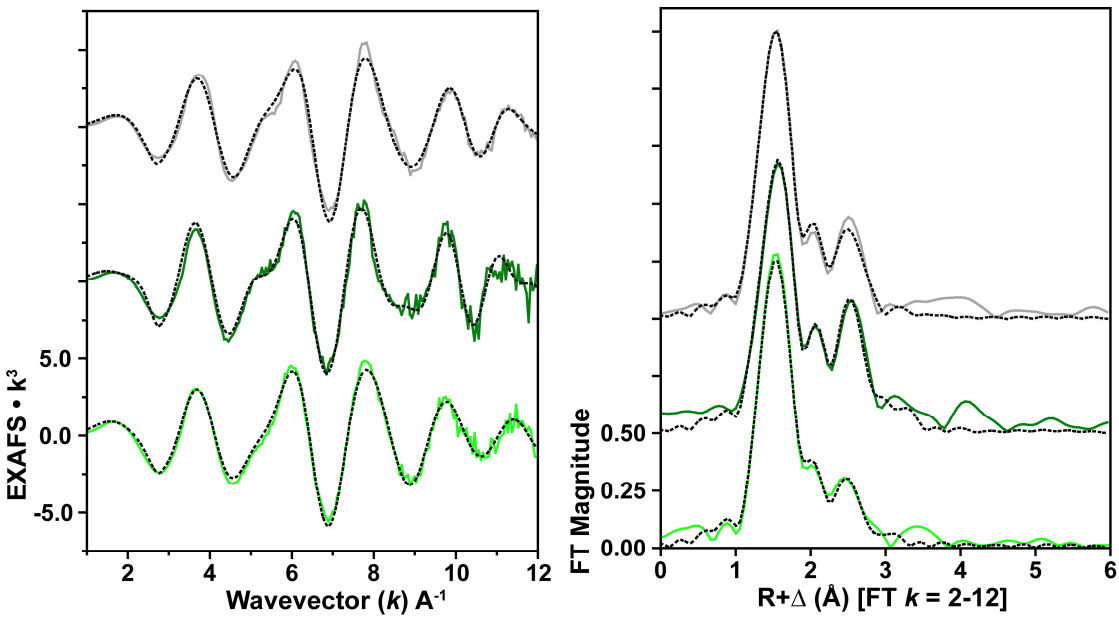


**Supplementary Figure 23.** EXAFS data (left) with Fourier transform (right) for $[Fe(IV)(TMC)(O)]^{2+}$ (**3**) acetone (light green), **3** acetonitrile (dark green), $[Fe(IV)(TMC)(O)(CH_3CN)]^{2+}$ (grey), data (—) and fit (----). Direct overlay of spectra is given in Supplementary Fig. 13, with fit values given in Supplementary Tables 7 and 8. The data quality of **3** in acetonitrile limited the fits to $k$ = 12 $Å^{-1}$ across the series.